GEOPHYSICS, VOL. 77, NO. 3 (MAY-JUNE 2012); P. U49–U62, 17 FIGS., 7 TABLES.
10.1190/GEO2011-0307.1

Moveout analysis of wide-azimuth data in the presence of lateral velocity variation

Mamoru Takanashi[1] and Ilya Tsvankin[2]

ABSTRACT

Moveout analysis of wide-azimuth reflection data seldom takes into account lateral velocity variations on the scale of spreadlength. However, velocity lenses (such as channels and reefs) in the overburden can cause significant, laterally varying errors in the moveout parameters and distortions in data interpretation. Here, we present an analytic expression for the normal-moveout (NMO) ellipse in stratified media with lateral velocity variation. The contribution of lateral heterogeneity (LH) is controlled by the second derivatives of the interval vertical traveltime with respect to the horizontal coordinates, along with the depth and thickness of the LH layer. This equation provides a quick estimate of the influence of velocity lenses and can be used to substantially mitigate the lens-induced distortions in the effective and interval NMO ellipses. To account for velocity lenses in nonhyperbolic moveout inversion of wide-azimuth data, we propose a prestack correction algorithm that involves computation of the lens-induced traveltime distortion for each recorded trace. The overburden is assumed to be composed of horizontal layers (one of which contains the lens), but the target interval can be laterally heterogeneous with dipping or curved interfaces. Synthetic tests for horizontally layered models confirm that our algorithm accurately removes lens-related azimuthally varying traveltime shifts and errors in the moveout parameters. The developed methods should increase the robustness of seismic processing of wide-azimuth surveys, especially those acquired for fracture-characterization purposes.

INTRODUCTION

The NMO (normal-moveout) ellipse obtained from P-wave conventional-spread data (with the maximum offset-to-depth ratio close to unity) provides valuable information for fracture interpretation and permeability modeling (e.g., Grechka and Tsvankin, 1999; Lynn, 2004a, b; Tsvankin et al., 2010; Tsvankin and Grechka, 2011). The major axis of the NMO ellipse often coincides with the dominant fracture azimuth and the direction of the maximum horizontal stress, while the eccentricity (the fractional difference between the axes) of the ellipse can be related to fracture density (Bakulin et al., 2000a; Jenner et al., 2001; Tod et al., 2007).

The NMO ellipse can be obtained by a "global" hyperbolic semblance search using all available offsets and azimuths (Grechka and Tsvankin, 1999) or by a trace-correlation approach (Jenner et al., 2001). To remove the influence of reflector dip, Calvert et al. (2008) apply so-called offset-vector tile binning described by Cary (1999) and Vermeer (2002), which preserves azimuthal information in time-migrated data. Application of azimuthal analysis in the depth-migrated domain is still uncommon, although it is possible to generate wide-azimuth image gathers after prestack depth migration (e.g., Melo and Sava, 2009; Sava and Vlad, 2011; Koren and Ravve, 2011).

With the advent of long-offset acquisition, analysis of the NMO ellipse has been supplemented by nonhyperbolic moveout inversion of multiazimuth data. The azimuthally varying quartic moveout coefficient in orthorhombic and HTI (transversely isotropic with a horizontal symmetry axis) media is controlled by the anellipticity coefficients $\eta^{(1)}$, $\eta^{(2)}$, and $\eta^{(3)}$ (Pech and Tsvankin, 2004; Vasconcelos and Tsvankin, 2006), which are sensitive to fracture compliances and orientations (Bakulin et al., 2000b). Although the kinematics of P-wave propagation in orthorhombic media with a

Manuscript received by the Editor 12 August 2011; revised manuscript received 1 December 2011; published online 30 April 2012.
[1]Colorado School of Mines, Department of Geophysics, Center for Wave Phenomena, Golden, Colorado, USA; Japan Oil, Gas and Metals National Corporation, Chiba, Japan. E-mail: takanashi-mamoru@jogmec.go.jp.
[2]Colorado School of Mines, Department of Geophysics, Center for Wave Phenomena, Golden, Colorado, USA. E-mail: ilya@dix.mines.edu.
© 2012 Society of Exploration Geophysicists. All rights reserved.

Downloaded 22 May 2012 to 138.67.12.93. Redistribution subject to SEG license or copyright; see Terms of Use at http://segdl.org/

fixed symmetry-plane orientation are controlled by six parameters (Tsvankin, 1997, 2005), only five of them (the symmetry-plane NMO velocities $V_{\rm nmo}^{(1,2)}$ and $\eta^{(1,2,3)}$) influence P-wave long-spread moveout (Vasconcelos and Tsvankin, 2006; Xu and Tsvankin, 2006). Vasconcelos and Tsvankin (2006) develop an efficient semblance-based algorithm to estimate the symmetry-plane orientation and five effective moveout parameters using the generalized Alkhalifah-Tsvankin nonhyperbolic equation. A stable technique to obtain the interval moveout parameters of orthorhombic media is presented by Wang and Tsvankin (2009), who implement the velocity-independent layer-stripping method (VILS) of Dewangan and Tsvankin (2006).

Anisotropic moveout analysis, however, is sensitive to correlated traveltime errors caused by near-surface heterogeneity or velocity lenses associated with channels and carbonate reefs (Luo et al., 2007; Jenner, 2009; Takanashi et al., 2009b). An analytic expression for the NMO ellipse in a horizontal layer with lateral velocity variation, introduced by Grechka and Tsvankin (1999), shows that the influence of lateral heterogeneity can be expressed through the curvature of the vertical traveltime surface. 2D modeling for layered VTI media in Takanashi and Tsvankin (2011) demonstrates that a velocity lens above the reflector can cause substantial, laterally varying errors in the NMO velocity and the anellipticity parameter η. In the presence of a lens, nonhyperbolic moveout inversion tends to produce even larger errors in $V_{\rm nmo}$ than does conventional analysis based on the hyperbolic moveout equation.

To correct for the influence of velocity lenses, Jenner (2010) suggests to use 3D tomographic inversion for laterally heterogeneous, azimuthally anisotropic models. Such an approach, however, is not only time-consuming but also requires accurate estimates of the overburden parameters. A 2D correction algorithm introduced in Takanashi and Tsvankin (2011) needs less a priori information, provided the lens is embedded in a horizontally layered overburden. Their algorithm computes lens-induced traveltime distortions for each trace separately using VILS.

Here, we study the influence of laterally varying velocity on azimuthal moveout analysis and develop correction algorithms for accurate anisotropic model-building. First, using the results of Grechka and Tsvankin (1999), we propose an approach designed to quickly estimate and remove the lens-related term in the effective and interval NMO ellipses. To mitigate lens-induced distortions in nonhyperbolic moveout inversion, we then extend the correction algorithm of Takanashi and Tsvankin (2011) to wide-azimuth data. Synthetic tests for layered HTI and orthorhombic media demonstrate that our techniques effectively restore the moveout function in the reference (laterally homogeneous) medium and provide accurate estimates of the background moveout parameters.

NMO ELLIPSE IN STRATIFIED LATERALLY HETEROGENEOUS MEDIA

Azimuthal variation of NMO velocity for pure (nonconverted) modes is typically elliptical, even if the medium is anisotropic and heterogeneous. The hyperbolic moveout equation for wide-azimuth data has the form (Grechka and Tsvankin, 1998)

$$t^2(h,\alpha) = t_0^2 + \frac{4h^2}{V_{\rm nmo}^2(\alpha)}, \tag{1}$$

where h is the half-offset, α is the azimuth of the CMP line, t_0 is the zero-offset traveltime, and $V_{\rm nmo}(\alpha)$ is the NMO velocity given by

$$V_{\rm nmo}^{-2}(\alpha) = W_{11}\cos^2\alpha + 2W_{12}\,\sin\,\alpha\,\cos\,\alpha + W_{22}\sin^2\alpha. \tag{2}$$

The symmetric 2×2 matrix W_{ij} depends on the second spatial derivatives of the one-way traveltime τ from the zero-offset reflection point to the surface location $\mathbf{x} = [x_1, x_2]$

$$W_{ij} = \tau_0 \left.\frac{\partial^2\tau}{\partial x_i\,\partial x_j}\right|_{\mathbf{x}=\mathbf{x}_{\rm CMP}}, \qquad (i,j=1,2); \tag{3}$$

τ_0 is the one-way zero-offset time. The matrix W_{ij} describes an ellipse if the eigenvalues of the matrix are positive (a typical case).

For a horizontal anisotropic layer with a horizontal symmetry-plane, the influence of weak lateral velocity variation on the NMO ellipse is represented by (Grechka and Tsvankin, 1999):

$$W_{ij}^{\rm hom} = W_{ij}^{\rm het} - \frac{\tau_0}{3}\left.\frac{\partial^2\tau_0}{\partial y_i\,\partial y_j}\right|_{\mathbf{y}=\mathbf{y}_{\rm CMP}}, \qquad (i,j=1,2), \tag{4}$$

where $W_{ij}^{\rm het}$ is the NMO ellipse in the laterally heterogeneous (LH) layer, $W_{ij}^{\rm hom}$ is the NMO ellipse for the reference homogeneous model, which has the same medium parameters as those at the CMP location, and $\tau_0 = \tau_0(\mathbf{y})$ is the one-way zero-offset traveltime at the surface location $\mathbf{y} = [y_1, y_2]$. The absence of the first derivatives of τ_0 indicates that a constant lateral gradient of the zero-offset traveltime (or a constant lateral gradient of the vertical slowness) does not distort the NMO ellipse, which is governed by quadratic lateral variation of τ_0 (Grechka and Tsvankin, 1999).

Equation 4 can be extended in a straightforward way to an arbitrary number of horizontal layers. We assume that lateral heterogeneity and anisotropy in each layer are weak and that the horizontal plane is a plane of symmetry. The same assumptions were made by Grechka and Tsvankin (1999, Appendix B) in their derivation of the NMO ellipse for a model with two LH layers. Following their approach, the NMO ellipse for the reflection from the bottom of an N-layered model can be obtained as (Appendix A):

$$W_{ij}^{\rm hom} = W_{ij}^{\rm het} - \sum_{m=1}^{N}\frac{\tau_0\,D_m}{3}\left.\frac{\partial^2\tau_{0m}}{\partial y_i\partial y_j}\right|_{\mathbf{y}=\mathbf{y}_{\rm CMP}}, \qquad (i,j=1,2), \tag{5}$$

where

$$D_m = k_m^2 + 3k_m l_m + 3l_m^2, \tag{6}$$

$$k_m = \frac{\tau_{0m}\left(V_{\rm cir}^{(m)}\right)^2}{\sum_{r=1}^{N}\tau_{0r}\left(V_{\rm cir}^{(r)}\right)^2}, \tag{7}$$

and

$$l_m = \frac{\sum_{r=m+1}^{N}\tau_{0r}\left(V_{cir}^{(r)}\right)^2}{\sum_{r=1}^{N}\tau_{0r}\left(V_{cir}^{(r)}\right)^2}. \tag{8}$$

Downloaded 22 May 2012 to 138.67.12.93. Redistribution subject to SEG license or copyright; see Terms of Use at http://segdl.org/

Here, τ_{0m} is the one-way interval vertical traveltime in layer m ($m = 1$ corresponds to the top layer), and the coefficients k_m and l_m in equations 7 and 8 can be obtained from interval moveout analysis. $V_{\rm cir}^{(m)}$ are the best-fit circles approximating the interval NMO ellipses for each layer (Grechka and Tsvankin, 1999):

$$V_{\rm cir}^{-2} = \frac{1}{2\pi}\int_0^{2\pi} V_{\rm nmo}^{-2}(\alpha)d\alpha = \frac{W_{11}^{\rm hom} + W_{22}^{\rm hom}}{2} \approx \frac{W_{11}^{\rm het} + W_{22}^{\rm het}}{2}. \tag{9}$$

The correction term in equation 5 is obtained by adding the contributions of all LH layers. If layer m is laterally homogeneous, the corresponding correction term goes to zero because the vertical time τ_{0m} is constant.

To study the dependence of the NMO ellipse on the depth and thickness of an LH interval in the overburden, we consider the special case of a three-layer medium with lateral velocity variation confined to the second layer (Figure 1). Using equation 5, the NMO ellipse for the reflection from the bottom of the model can be written as:

$$W_{ij}^{\rm hom} = W_{ij}^{\rm het} - \frac{\tau_0 D}{3}\frac{\partial^2 \tau_{02}}{\partial y_i\, \partial y_j}\bigg|_{\mathbf{y}=\mathbf{y}_{\rm CMP}}, \qquad (i,j = 1,2), \tag{10}$$

where

$$D = k^2 + 3kl + 3l^2, \tag{11}$$

$$k = \frac{\tau_{02}(V_{\rm cir}^{(2)})^2}{\tau_{01}(V_{\rm cir}^{(1)})^2 + \tau_{02}(V_{\rm cir}^{(2)})^2 + \tau_{03}(V_{\rm cir}^{(3)})^2}, \tag{12}$$

and

$$l = \frac{\tau_{03}(V_{\rm cir}^{(3)})^2}{\tau_{01}(V_{\rm cir}^{(1)})^2 + \tau_{02}(V_{\rm cir}^{(2)})^2 + \tau_{03}(V_{\rm cir}^{(3)})^2}. \tag{13}$$

If the vertical velocity variation is weak, k and l are close to the relative thicknesses of the second and third layers, respectively. When $l = 0$, the model includes just an LH layer overlaid by a homogeneous medium, and the term D reduces to k^2. This result, obtained by Grechka and Tsvankin (1999), indicates that the influence of a thin LH layer located immediately above the target reflector is insignificant. Indeed, when the relative thickness of the LH layer is 0.1, the term D reduces to just 0.01 (equations 10 and 11 and Figure 2), compared to unity for a single LH layer (equation 4).

However, the influence of LH rapidly increases with the thickness of layer 3 and reaches its maximum when the LH layer is located at the top of the model (the term D reaches 2.71 when $k = 0.1$ and $l = 0.9$). Indeed, the contribution of a thin LH layer to the NMO ellipse is proportional to the squared relative thickness of the third (underlying) layer because the term $3l^2$ in equation 11 makes the primary contribution to D when $l \gg k$. Thus, along with the thickness of the LH layer, its distance from the target reflector is a key parameter responsible for the LH-induced distortion.

For a fixed depth of the LH layer, the magnitude of the LH-related term in equation 10 increases with target depth not only because of a larger coefficient D, but also because of the increase in the total vertical traveltime τ_0. As illustrated by Figure 3, the NMO-velocity error monotonically increases with the depth of the target reflector and also with the velocity in the third (deepest) layer or elsewhere in the medium. Indeed, $W_{ij}^{\rm hom}$ is inversely propotional to the squared average velocity ($V_{\rm avg}$) in the model, while τ_0 in the LH-related term in equation 10 is proportional $1/V_{\rm avg}$. Therefore, the contribution of the correction term increases with the average velocity.

The exact interval NMO ellipse in the reference laterally homogeneous medium can be found from the generalized Dix equation (Grechka et al., 1999):

$$\mathbf{W}_{n,\rm hom}^{-1} = \frac{t(N)\mathbf{W}_{\rm hom}^{-1}(N) - t(N-1)\mathbf{W}_{\rm hom}^{-1}(N-1)}{t(N) - t(N-1)}, \tag{14}$$

where $\mathbf{W}_{\rm hom}(N-1)$ and $\mathbf{W}_{\rm hom}(N)$ describe the reference effective NMO ellipses for the top and bottom of the Nth layer (respectively), and $t(N-1)$ and $t(N)$ are the corresponding zero-offset traveltimes. When the target interval is located beneath the LH layer, the LH-induced distortion in $\mathbf{W}_{\rm het}(N)$ is larger than that in $\mathbf{W}_{\rm het}(N-1)$ (see Figure 3). Hence, substitution of $\mathbf{W}_{\rm het}$ for

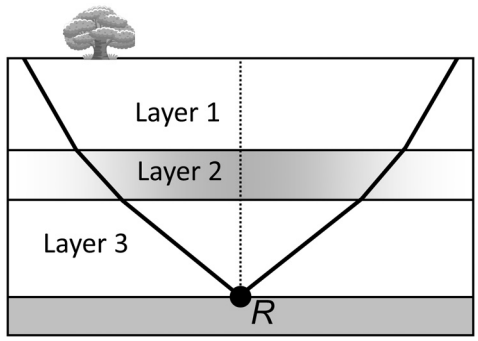

Figure 1. Reflection raypath through a model with three horizontal layers. Here, R is the reflection point for the unperturbed ray. Following Grechka and Tsvankin (1999), the raypath perturbation caused by weak lateral heterogeneity is assumed to be negligible, and the ray is confined to the vertical plane. Only the second layer is laterally heterogeneous.

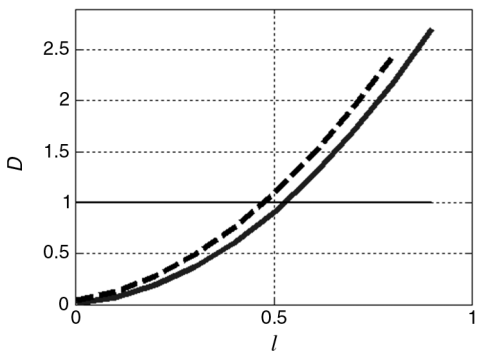

Figure 2. Coefficient D for a three-layer model computed from equation 11 as a function of the parameter l for $k = 0.1$ (solid line) and $k = 0.2$ (dashed). Here, $D = 1$ (thin horizontal line) corresponds to a single LH layer. For $l = 0$, the reflector coincides with the bottom of the LH layer.

Downloaded 22 May 2012 to 138.67.12.93. Redistribution subject to SEG license or copyright; see Terms of Use at http://segdl.org/

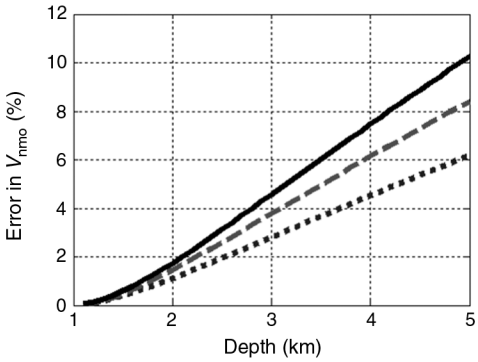

Figure 3. LH-induced distortion in the effective NMO velocity computed from equation 10 in the y-direction for a three-layer isotropic model where lateral heterogeneity is confined to the second layer. The horizontal axis is the depth of the target interface (the bottom of the third layer). The velocity at the CMP location ($y = 0$ km) in the first and second layers is 3 km/s, and in the third layer is 2 km/s (dotted line), 3 km/s (dashed) and 4 km/s (solid). The second (LH) layer is located at 1 km depth with thickness $z_2 = 0.2$ km and $\partial^2\tau_{02}/\partial y^2 = 0.02$ s/km^2, which corresponds to a 10 ms perturbation of τ_{02} (or a 13% velocity perturbation) at $y = \pm 1$ km. There is no linear lateral velocity variation in the LH layer.

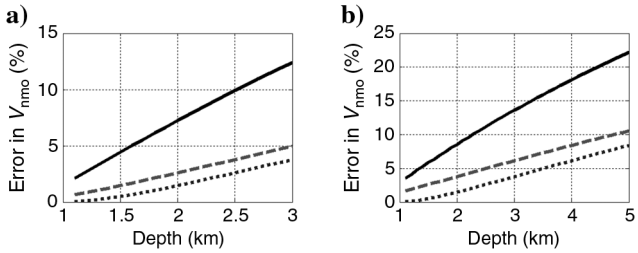

Figure 4. LH-induced distortion in the interval NMO velocity (solid line) for a horizontally layered isotropic model where the thickness of the target interval is (a) 0.5 km and (b) 1 km. The horizontal axis is the depth of the top of the target interval. The velocity at the CMP location ($y = 0$ km) is 3 km/s for all depths, and an LH layer is located at 1 km depth with thickness $z_2 = 0.2$ km and $\partial^2\tau_{02}/\partial y^2 = 0.02$ s/km^2 (the other layers are laterally homogeneous). Here, V_{nmo} is computed in the y-direction using Dix differentiation. Errors in the effective NMO velocities for the top (dotted) and bottom (dashed) of the target layer are shown for comparison.

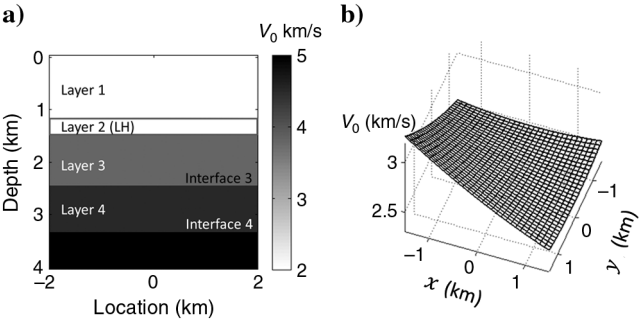

Figure 5. (a) Stratified HTI model that includes an isotropic LH layer. (b) Lateral variation of the vertical velocity V_0 in the LH layer. Model parameters are listed in Table 1.

$\mathbf{W}_{hom}$ causes errors in the interval NMO ellipse obtained from equation 14. Although the difference in the correction term between $\mathbf{W}_{het}(N)$ and $\mathbf{W}_{het}(N-1)$ may be relatively small if the Nth layer is thin, the influence of LH is amplified by Dix differentiation (Figure 4). Therefore, the NMO ellipse should be corrected for lateral heterogeneity before applying equation 14.

Similar conclusions for isotropic media are drawn by Blias (2009), who shows that the heterogeneity-related distortion becomes more significant after Dix differentiation. Note that our algorithm can be applied to NMO velocities estimated from 2D data and, therefore, can increase the accuracy of conventional velocity analysis and time-to-depth conversion based on the Dix equation.

Synthetic test

Next, we compare analytic NMO ellipses computed from equations 10–14 with the ellipses reconstructed from synthetic data generated by a 2D finite-difference algorithm (we used the open-source Madagascar code "sfewe"). The model includes an isotropic LH interval embedded in a layered HTI medium (Figure 5 and Table 1).

HTI can be considered as a special case of the more general orthorhombic medium with a horizontal symmetry plane. The azimuthal variation of the P-wave NMO velocity in a horizontal orthorhombic layer is described by (Tsvankin, 1997, 2005):

$$V_{nmo}^{-2}(\alpha) = \frac{\sin^2(\alpha-\varphi)}{[V_{nmo}^{(1)}]^2} + \frac{\cos^2(\alpha-\varphi)}{[V_{nmo}^{(2)}]^2}, \qquad (15)$$

$$V_{nmo}^{(i)} = V_0\sqrt{1+2\delta^{(i)}}, \quad (i=1,2), \qquad (16)$$

where φ is the azimuth of the symmetry plane $[x_1, x_3]$, $V_{nmo}^{(1,2)}$ are the symmetry-plane NMO velocities, and $\delta^{(1,2)}$ are the anisotropy parameters introduced by Tsvankin (1997). For an HTI layer with the symmetry axis x_1, the coefficient $\delta^{(1)} = 0$, and the NMO ellipse is determined by the parameters V_0, φ, and $\delta^{(2)}$ (often denoted by $\delta^{(V)}$). Equation 15 remains valid in a layered HTI or orthorhombic medium with a uniform orientation of the vertical symmetry planes. The velocities $V_{nmo}^{(1,2)}$ then become effective parameters obtained by rms averaging of the interval values.

The isotropy plane of the HTI layers ($\varphi = 45°$) represents a plane of symmetry for the entire model. Although the orthogonal plane is not a plane of symmetry, our testing shows that the NMO ellipses can be accurately estimated by 2D synthetic modeling and hyperbolic semblance search for the vertical planes corresponding to $\varphi = \pm 45°$. The interval NMO ellipses are then obtained from

Table 1. Parameters of the model from Figure 5. The vertical velocity V_0 in layer 2 is shown in Figure 5b. The Thomsen-style parameter $\delta^{(V)}$ is defined in the symmetry-axis plane of HTI media (e.g., Tsvankin, 2005), and φ is the azimuth of the symmetry axis.

	Layer 1	Layer 2	Layer 3	Layer 4
V_0 (km/s)	2.0	2.5–3.2	3.8	4.5
$\delta^{(V)}$	−0.05	0	−0.03	−0.07
φ (degrees)	−45	—	−45	−45

Downloaded 22 May 2012 to 138.67.12.93. Redistribution subject to SEG license or copyright; see Terms of Use at http://segdl.org/

the generalized Dix equation 14 without correcting for lateral heterogeneity. The analytic NMO ellipses W_{ij}^{het} are computed from the second derivatives of the interval traveltime τ_{02} at the CMP location and the exact expression for the reference ellipses W_{ij}^{hom}. Since the surface $\tau_{02}(x_1, x_2)$ for the LH layer from the model in Figure 5 is sufficiently smooth, the second traveltime derivative $\partial^2\tau_{02}/(\partial y_i \partial y_j)$ can be accurately evaluated in a close vicinity (1×1 km) of the CMP location.

The difference in the eccentricity of the NMO ellipses computed by the two methods does not exceed 2% (Table 2). This test also confirms that the distortion caused by an LH layer in the overburden increases with reflector depth and is further amplified by Dix-type differentiation (Table 2). The eccentricity of the interval NMO ellipse for layer 4 determined from the synthetic data is more than two times greater than the actual value. The error in the interval eccentricity reduces from 12.5% to 2% when the correction term is subtracted from the effective NMO ellipses (equation 5) prior to Dix differentiation (equation 14).

Next, we investigate the sensitivity of the presented analytic approach to the strength of anisotropy and lateral heterogeneity using the model in Figure 5. When the values of $\delta^{(V)}$ for layers 1, 3, and 4 are changed to 0.15, 0.09, and 0.21, respectively (the other parameters are the same as in Table 1), the error of equation 5 for the eccentricity of the effective NMO ellipses is still less than 2%, although the interval eccentricity is distorted by 5%. If the magnitude of the lateral velocity variation in the LH layer (layer 2) is three times larger than that for the model in Figure 5, the difference between the analytic and numerical estimates of the effective eccentricity does not exceed 3%, with the corrected interval eccentricity deviating by 5% from the actual value.

ESTIMATION OF THE LENS-INDUCED DISTORTION IN NMO ELLIPSES

Here, we explore the possibility of applying the above formalism to evaluation of distortions caused by a velocity lens. First, following Biondi (2006) and Takanashi and Tsvankin (2011), we review the influence of a high-velocity lens on the NMO velocity for 2D models where the effective spreadlength L' (i.e., the maximum distance between the incident and reflected rays at lens depth) is larger than the lens width (Figure 6a). At the center of the lens (location B), the NMO velocity is significantly reduced compared to that for the background medium (location A) because of a larger traveltime difference between the near- and far-offset traces. At the side of the lens (location C), V_{nmo} is greater than the background value. A similar distortion in V_{nmo} can also be induced by a horst structure when the overburden has a lower velocity (Figure 6b).

The 2D analysis helps understand the influence of a velocity lens on the NMO ellipse. We consider a 3D model containing an elongated high-velocity lens embedded in a homogeneous background layer (Figure 7). The NMO velocity estimated at location B in the direction perpendicular to the lens is smaller than the background value. The NMO velocity parallel to the lens represents the correct effective V_{nmo} (provided the lens is longer than the effective spreadlength), which is slightly higher than the velocity in the background. Thus, the NMO ellipse at point B is extended in the direction parallel to the lens. Near the edge of the lens (location C), the NMO velocity measured perpendicular to the lens is greater than V_{nmo} in the background.

Therefore, if the background is isotropic, the major axis of the NMO ellipse is parallel to the high-velocity lens at location B and perpendicular to it at location C (Figure 7a). If the background is azimuthally anisotropic with the high-velocity direction perpendicular to the lens, the NMO ellipse becomes closer to a circle at location B and more elongated at location C (Figure 7b). The spatially varying NMO ellipses in Figure 7b resemble those observed on field data by Takanashi et al. (2009b), who attributed

Table 2. Eccentricity of the effective NMO ellipses (described by W_{ij}^{het}) for interfaces 3 and 4 and of the interval NMO ellipse in layer 4 for the model in Figure 5 and Table 1. The analytic values computed from equation 5 are compared with those obtained by synthetic modeling. The interval NMO ellipses are found from equation 14 without correcting for lateral heterogeneity. The background eccentricity corresponds to the reference laterally homogeneous model at the CMP location. The azimuth of the major axis of all NMO ellipses is 45°.

	Interface 3	Interface 4	Interval (layer 4)
Analytic (%)	7.3	12	18
Numerical (%)	8.1	13	20
Background (%)	3.5	4.9	7.5

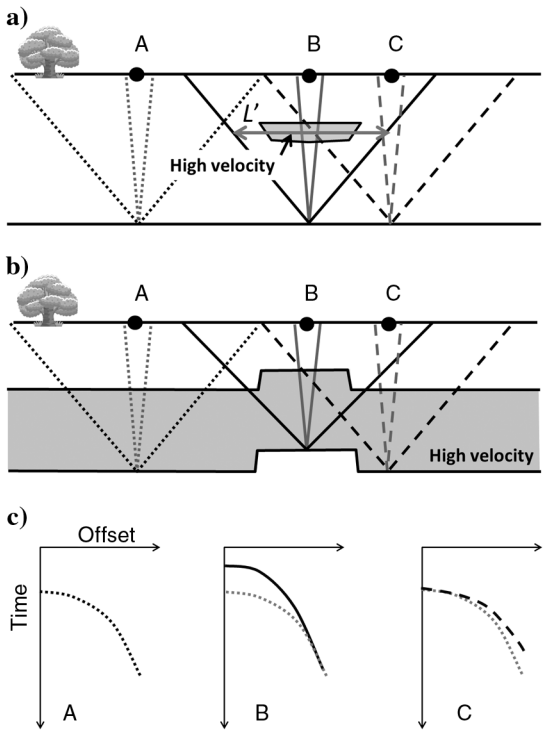

Figure 6. Schematic picture of near- and far-offset raypaths from a horizontal reflector beneath (a) a high-velocity lens and (b) a horst structure where the top layer has a lower velocity (modified from Biondi, 2006, and Takanashi and Tsvankin, 2011). (c) The influence of the lens or horst structure on the moveout curves. The raypaths and moveout curves at locations A, B, and C are shown by dotted, solid, and dashed lines, respectively.

Downloaded 22 May 2012 to 138.67.12.93. Redistribution subject to SEG license or copyright; see Terms of Use at http://segdl.org/

the NMO-velocity distortions to the presence of a high-velocity lens in the overburden.

Next, we apply equation 5, designed for a smooth velocity field, to correct for the influence of a velocity lens embedded in horizontally layered media. Grechka and Tsvankin (1999) show that accurate estimation of the second traveltime derivatives in an LH layer generally requires spatial smoothing and the order of the polynominal used to approximate $\tau_0(x, y)$ influences the correction results.

Here, we suggest to compute the curvature of the interval vertical traveltime in a spreadlength-dependent way to adequately approximate lens-induced distortions in the NMO ellipse using equation 5. The finite-spread moveout velocity is primarily governed by the lateral variation of the interval vertical traveltime over the area corresponding to the effective spreadlength $L'(\alpha)$ (α is the azimuth). Ignoring ray bending, $L'(\alpha)$ can be found as

$$L'(\alpha) = \frac{Z - Z'}{Z} L(\alpha), \tag{17}$$

where $L(\alpha)$ is the spreadlength, Z is the reflector depth, and Z' is the depth of the lens. As shown below, $L'(\alpha)$ can be accurately estimated by velocity-independent layer-stripping (VILS) without knowledge of the medium parameters. The lateral variation of τ_{02} over $L'(\alpha)$ can be approximated by the quadratic equation

$$\tau_{02}(x, y) = a + bx + cy + dx^2 + exy + fy^2, \tag{18}$$

and the second derivatives of τ_{02} then become

$$\frac{\partial^2 \tau_{02}}{\partial x^2} = 2d, \quad \frac{\partial^2 \tau_{02}}{\partial x \partial y} = e, \quad \frac{\partial^2 \tau_{02}}{\partial y^2} = 2f. \tag{19}$$

The best-fit curvature (i.e., the coefficients d, e, and f) obtained from equation 18 can vary with spreadlength; a larger spreadlength generally reduces the estimated curvature. Since $L'(\alpha)$ increases with target depth (Takanashi and Tsvankin, 2011), the computed curvature is also depth-dependent. The parameters d, e, and f, combined with τ_0 and D, are sufficient to compute the correction terms in equation 5 at a given CMP location. The synthetic test below confirms that this method accurately approximates the distortion in the NMO ellipse caused by a lens with a width (w) smaller than L'. If the lens is centered at the CMP location, the curvature is substantial for the ratio w/L' ranging between 0.3 and 0.7, which is consistent with 2D numerical results in Takanashi and Tsvankin (2011).

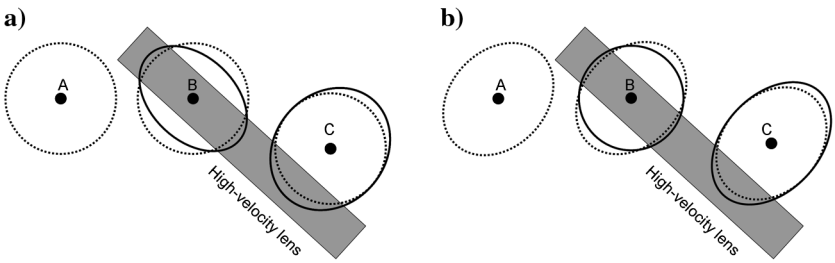

Figure 7. Plan view of NMO ellipses (solid lines) at three locations for an otherwise homogeneous layer with an embedded high-velocity elongated lens (shaded). The velocity model and raypaths in the vertical plane perpendicular to the lens are the same as in Figure 6a. The lens is embedded in (a) an isotropic background and (b) an azimuthally anisotropic background with the higher-velocity direction perpendicular to the major axis of the lens. The dashed circles mark the background NMO ellipses at location A outside the lens.

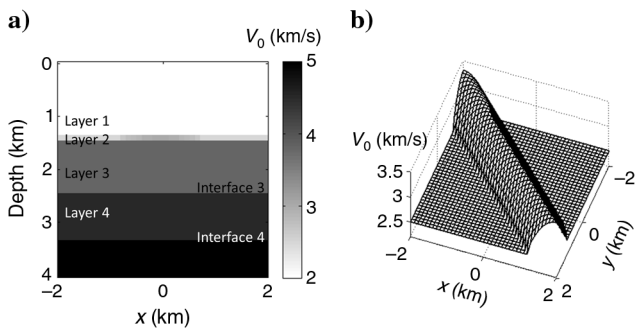

Figure 8. (a) Isotropic layered model with an elongated high-velocity lens. The first, third, and fourth layers are homogeneous with $V_0 = 2$ km/s, 3.8 km/s, and 4.5 km/s, respectively. (b) The velocity surface in the second layer, which is 100 m thick and contains a smooth elongated lens with $V_0 = 3.3$ km/s at the center ($V_0 = 2.5$ km/s outside the lens).

Synthetic tests

Isotropic model with an elongated lens

First, we present a synthetic example for a multilayered isotropic model that contains a high-velocity elongated lens in the second layer (Figure 8). The lens-induced vertical-traveltime distortion reaches 20 ms. Using equations 5–8 and 17–19, we analyze the influence of the lens on the effective and interval NMO ellipses.

To obtain the correction term in equation 5 for interfaces 3 and 4, we estimate the curvature of the interval vertical traveltime τ_{02}. The best-fit surface of τ_{02}, obtained from equation 18 for the area of the effective spread L', has a positive curvature (in the direction perpendicular to the lens axis) at the center of the lens and a negative curvature outside it. When the horizontal distance between the lens and the CMP location is larger than half the effective spreadlength, the curvature goes to zero.

In agreement with Figure 7a, the matrix W_{ij}^{het} computed from equations 5–8 and 17–19 shows that the major axis of the effective NMO ellipses for interfaces 3 and 4 is parallel to the lens axis at the center of the lens and perpendicular to it outside the lens (Figure 9). The larger distortion for interface 4 is due to an increase in τ_0 and the coefficient D with depth (equation 10).

Although the target interval is isotropic and located far below the thin LH layer, applying Dix-type differentiation without correcting for the influence of the lens amplifies the false elongation of the effective NMO ellipses (Figure 9). The false eccentricity of the interval NMO ellipse reaches 10%, which exceeds a typical anisotropy-related azimuthal variation of V_{nmo} (e.g., Grechka and Tsvankin, 1999).

Downloaded 22 May 2012 to 138.67.12.93. Redistribution subject to SEG license or copyright; see Terms of Use at http://segdl.org/

Table 3 compares the NMO ellipses computed from equation 5 with the ellipses reconstructed from wide-azimuth synthetic data (generated with finite-differences) using the global semblance search of Grechka and Tsvankin (1999). The eccentricity of the analytic NMO ellipses for both interfaces does not deviate by more than 1% from the numerically modeled value. Therefore, equation 5 gives an accurate description of NMO ellipses in a layered isotropic medium with a thin elongated lens.

Jenner's model

A more complicated isotropic model with lateral heterogeneity is studied by Jenner (2009; Figure 10). The lateral velocity variation is produced by the topography of the top of a low-velocity inclusion inside the LH layer; the maximum push-down vertical time anomaly is 16 ms (Figure 10b). Using ray-traced synthetic data of Jenner (2009), we compared the NMO ellipses obtained by hyperbolic moveout inversion with those computed from equations 5–8.

As expected, the NMO ellipses for interfaces 1 and 2 are extended perpendicular to the axis of the low-velocity lens above the lens center and parallel to the axis outside the lens. Similar to the model from Figures 8 and 9, the distortion of the effective NMO ellipses is larger for the deeper interface (Figure 11). The effective eccentricity for Jenner's model is small because the LH layer is located relatively close to the two deeper reflectors (see equations 5 and 6). However, the false azimuthal variation of the effective NMO velocity is significantly amplified in the interval NMO ellipses obtained from Dix differentiation (Figure 12). Although the zero-offset traveltime surface in the LH layer has a complicated shape, and the semblance for CMP locations near the lens is relatively low, the analytic ellipses are in good agreement with those reconstructed from the synthetic data. Note that the magnitude of the interval eccentricity (both analytic and modeled numerically) does not increase with depth as rapidly as it does in Figure 4; indeed, the estimated curvature (i.e., the magnitude of the parameters d, e, and f in equation 18) in equation 5 decreases with target depth.

HTI model

Next, we examine an azimuthally anisotropic medium (Table 4) that has the same geometry as the isotropic model in Figure 8. The LH layer is kept isotropic, while the other layers have HTI symmetry. The effective NMO ellipses computed from equation 5 are close to circles at the center of the lens because the influence of azimuthal anisotropy is compensated by the lens-induced distortion (Figure 13a, b). Substantial effective and interval ellipticities are observed at the side of the lens where LH further stretches the NMO ellipse for the reference homogeneous model. As is the case for isotropic media, the LH-induced distortion is amplified in the interval NMO ellipses (Figure 13c).

To verify the accuracy of the analytic expressions, we reconstruct the interval NMO ellipses in layer 4 using finite-difference synthetic data. Since lateral heterogeneity and azimuthal anisotropy are relatively weak, reflection traveltimes in any azimuthal direction are well-approximated by those computed using the 2D finite-difference algorithm, as was confirmed by comparing shot

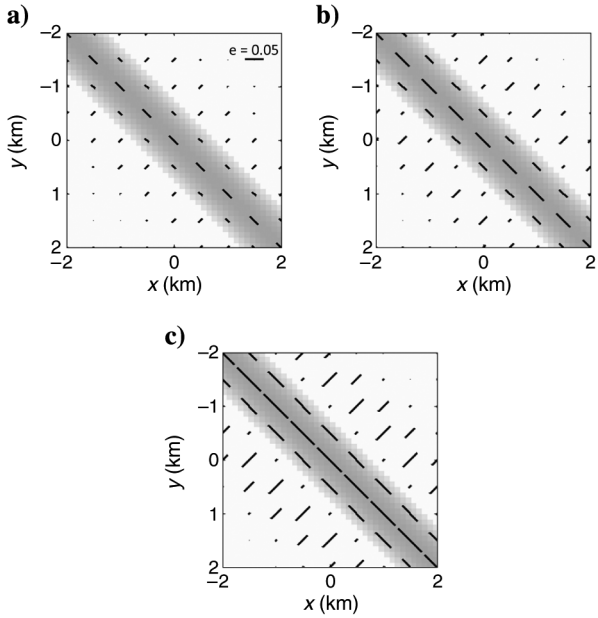

Figure 9. Effective NMO ellipses for the model from Figure 8 (the gray zone marks the lens, see Figure 8b) for interfaces (a) 3 and (b) 4. (c) The interval NMO ellipses for layer 4 obtained by generalized Dix differentiation without correcting for lateral heterogeneity. The ticks are parallel to the major axis of the ellipse, and their length is proportional to the eccentricity. The maximum eccentricity (at the center of the lens) is 4%, 6%, and 10% for plots (a), (b), and (c), respectively. The spreadlength is 3 km in both the x- and y-directions.

Table 3. Comparison of the eccentricity of the NMO ellipses computed from equations 5–8 and 17–19 with that obtained from finite-difference synthetic data for the model from Figure 8.

CMP location (x, y) km	Interface 3 (0, 0)	Interface 3 (0, 1.5)	Interface 4 (0, 0)	Interface 4 (0, 1.5)
Analytic (%)	4.4	2.5	6.4	3.5
Finite-difference (%)	4.9	1.6	7.0	3.4

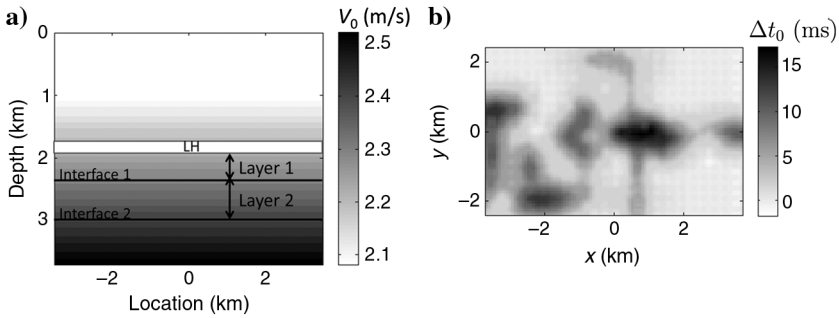

Figure 10. (a) Isotropic layered model with a 200 m-thick laterally heterogeneous layer (Jenner, 2009). (b) Zero-offset time distortion (estimated from the push-down anomaly on the near-offset stack) caused by a low-velocity inclusion in the LH layer.

Downloaded 22 May 2012 to 138.67.12.93. Redistribution subject to SEG license or copyright; see Terms of Use at http://segdl.org/

gathers produced by 2D and 3D modeling. To remove the LH-induced distortion in the effective NMO ellipses, we estimate the coefficient D in equation 5 from the zero-offset traveltime τ_0 and the best-fit azimuthally invariant NMO velocity (i.e., the "NMO circle") for each layer. Because the model is horizontally layered, the zero-offset time distortion $\Delta\tau_0$ can be accurately recovered from the pull-up anomaly on the near-offset stacked section. The second derivatives of the interval vertical traveltime are then obtained from the best-fit surface τ_{02} over the area limited by the effective spreadlength using equation 18.

The interval NMO ellipse estimated from the uncorrected data is strongly distorted by LH both at the center and outside the lens (Table 5). The eccentricity is understated at the center of the lens and overstated outside, and the major axis of the ellipse at the center of the lens is even rotated by 90°. For the model parameters in Table 4, the major axis after the correction has the correct orientation and the error in the eccentricity is less than 1%. Furthermore, the correction accurately reconstructs the background NMO ellipse for a medium with stronger azimuthal anisotropy (model 2); the error in the eccentricity at the center of the lens for that model decreases from 11% to 2%.

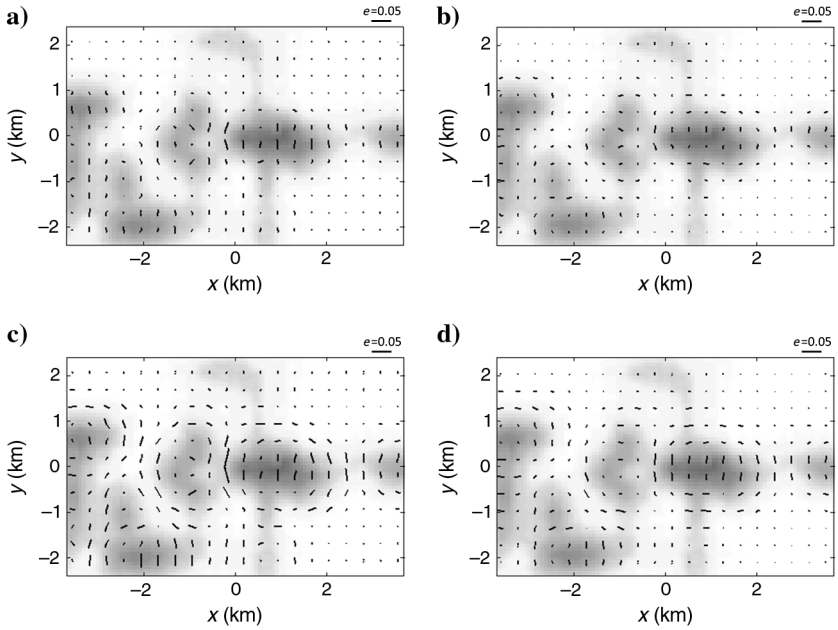

Figure 11. Effective NMO ellipses for interfaces (a, b) 1 and (c, d) 2 from the model in Figure 10 obtained from (a, c) hyperbolic moveout inversion and (b, d) equations 5–8 and 17–19. The spreadlength-to-depth ratio for moveout analysis is unity. The gray scale is proportional to the magnitude of the zero-offset time distortion (see Figure 10b).

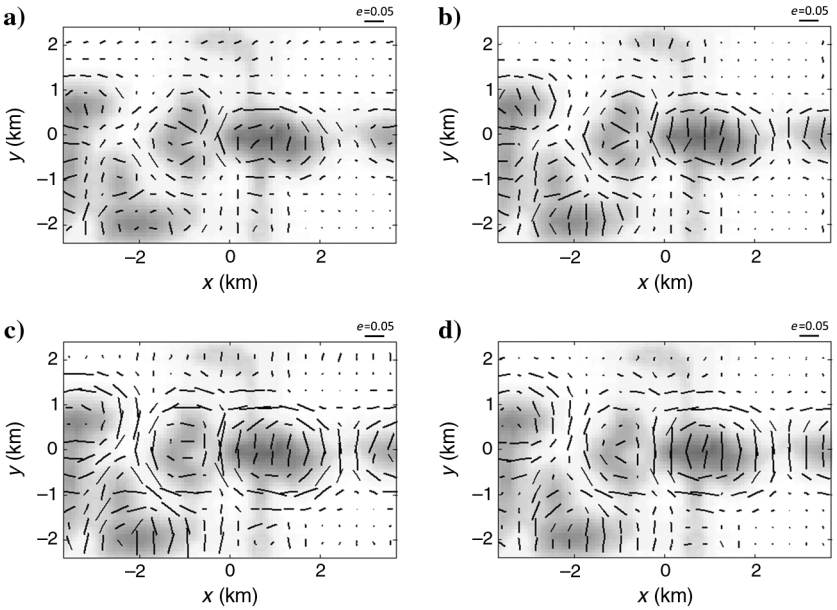

Figure 12. Interval NMO ellipses for layers (a, b) 1 and (c, d) 2 obtained from (a, c) hyperbolic inversion and (b, d) equations 5–8 and 17–19. The interval ellipses are computed from the generalized Dix equation without correcting for lateral heterogeneity.

LENS CORRECTION FOR NONHYPERBOLIC MOVEOUT INVERSION OF WIDE-AZIMUTH DATA

For a horizontal, laterally homogeneous orthorhombic layer with a horizontal symmetry plane, long-spread P-wave reflection moveout is accurately described by the generalized Alkhalifah-Tsvankin (1995) equation (Xu and Tsvankin, 2006; Tsvankin and Grechka, 2011)

$$t^2 = t_0^2 + \frac{x^2}{V_{\rm nmo}^2(\alpha)} - \frac{2\,\eta(\alpha)\,x^4}{V_{\rm nmo}^2[t_0^2\,V_{\rm nmo}^2(\alpha) + (1+2\eta(\alpha))x^2]}, \tag{20}$$

where t is the traveltime as a function of the offset x and azimuth α, and t_0 is the zero-offset time. The azimuthally varying NMO velocity (the NMO ellipse) is given by equation 15, while the azimuthally varying parameter $\eta(\alpha)$ can be found from (Pech and Tsvankin, 2004):

$$\eta(\alpha) = \eta^{(1)}\sin^2(\alpha-\varphi) - \eta^{(3)}\sin^2(\alpha-\varphi)\cos^2(\alpha-\varphi) + \eta^{(2)}\cos^2(\alpha-\varphi); \tag{21}$$

φ is the azimuth of the $[x_1, x_3]$ symmetry plane, and the anellipticity parameters $\eta^{(1,2,3)}$ are defined in the symmetry planes.

Equation 20 remains sufficiently accurate for horizontally layered orthorhombic media, if $V_{\rm nmo}(\alpha)$ represents the effective NMO ellipse, and the effective η for each azimuth is given by the VTI equation (Xu and Tsvankin, 2006):

Downloaded 22 May 2012 to 138.67.12.93. Redistribution subject to SEG license or copyright; see Terms of Use at http://segdl.org/

$$\eta(\alpha) = \frac{1}{8}\left\{\frac{1}{V_{\mathrm{nmo}}^4(\alpha)t_0}\left[\sum_{i=1}^{N}\left(V_{\mathrm{nmo}}^{(i)}(\alpha)\right)^4 \times (1+8\eta^{(i)}(\alpha))t_0^{(i)}\right] - 1\right\}, \quad (22)$$

where $V_{\mathrm{nmo}}^{(i)}$ and $\eta^{(i)}(\alpha)$ are the interval parameters. The principal azimuthal directions for the effective parameter $\eta(\alpha)$ in equation 21 are described by a separate angle φ_1 (rather than φ), if the vertical symmetry planes in different layers are misaligned (Xu and Tsvankin, 2006). The symmetry-plane orientation and five effective moveout parameters can be obtained by a semblance-based algorithm using the nonhyperbolic equation 20 (Vasconcelos and Tsvankin, 2006). After the effective traveltimes have been reconstructed, the velocity-independent layer-stripping method (VILS) can be employed to find the interval moveout parameters (Wang and Tsvankin, 2009).

Correction algorithm

To remove the influence of lenses on long-offset reflection traveltime, we extend the correction algorithm of Takanashi and Tsvankin (2011) to 3D wide-azimuth data. Eliminating the traveltime distortions on each recorded trace ensures accurate estimation of the moveout parameters in equations 20 and 21. This extension is based on the 3D version of VILS employed by Wang and Tsvankin (2009) (also, see Tsvankin and Grechka, 2011) for purposes of interval nonhyperbolic moveout inversion in laterally homogeneous media. As is the case for the 2D algorithm, the lens should be embedded in a horizontally layered overburden, but the target layer can be heterogeneous with dipping or curved internal reflectors (Figure 14).

Under the assumption that the raypath perturbation caused by the lens is negligible, VILS can estimate the horizontal coordinates $\mathbf{x}_{T1}$, $\mathbf{x}_{R1}$, $\mathbf{x}_{T2}$, and $\mathbf{x}_{R2}$ of the intersection points along the raypath. This procedure does not require knowledge of the velocity model and involves matching the time slopes of the target event and those of the reflections from the top and bottom of the layer containing the lens (Figure 14a, see Wang and Tsvankin, 2009). Then, ignoring ray bending in the lens layer, we can find the horizontal coordinates of the crossing points and the ray angles (Figure 14):

$$\mathbf{x}_{TL} = \mathbf{x}_{T1} + \frac{z'_{TL}(\mathbf{x}_{T2} - \mathbf{x}_{T1})}{z}, \quad (23)$$

$$\mathbf{x}_{RL} = \mathbf{x}_{R1} + \frac{z'_{RL}(\mathbf{x}_{R2} - \mathbf{x}_{R1})}{z}, \quad (24)$$

$$\cos\theta_{TL} = \frac{z}{\sqrt{|\mathbf{x}_{T1} - \mathbf{x}_{T2}|^2 + z^2}}, \quad (25)$$

$$\cos\theta_{RL} = \frac{z}{\sqrt{|\mathbf{x}_{R1} - \mathbf{x}_{R2}|^2 + z^2}}, \quad (26)$$

where z is the layer thickness, and z'_{TL} and z'_{RL} are the distances between the lens and the top of the layer at locations $\mathbf{x}_{TL}$ and $\mathbf{x}_{RL}$, respectively.

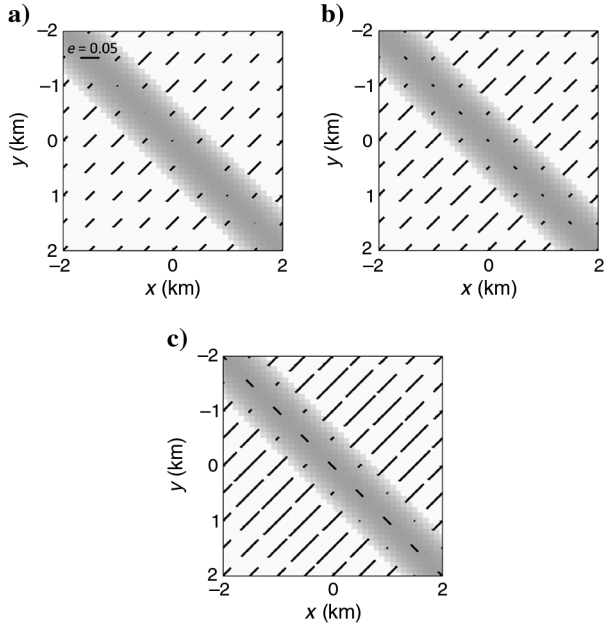

Figure 13. Effective NMO ellipses (same display as in Figure 9) for interfaces (a) 3 and (b) 4 from the layered HTI model in Table 4. (c) The interval NMO ellipses for layer 4 obtained from the generalized Dix equation. The maximum eccentricity is 5%, 8%, and 13% for plots (a), (b), and (c), respectively. The eccentricity of the effective background NMO ellipses for interfaces 3 and 4 is 3.8% and 5.1%, respectively.

Table 4. Relevant parameters of the HTI model used in synthetic testing. The model geometry and the vertical velocity V_0 are the same as in Figure 8. The second (LH) layer is isotropic with V_0 shown in Figure 8b; the other layers are laterally homogeneous.

	Layer 1	Layer 2	Layer 3	Layer 4
V_0 (km/s)	2.0	2.5–3.2	3.8	4.5
$\delta^{(V)}$	−0.05	0	−0.03	−0.07
φ (degrees)	−45	—	−45	−45

Table 5. Eccentricity of the interval NMO ellipses in layer 4 of the four-layer HTI medium from Table 4. The ellipses are obtained by generalized Dix differentiation before and after correcting for lateral heterogeneity. The parameters of model 1 are listed in Table 4 (see also Figure 13), while for model 2 the parameter $\delta^{(V)}$ in layer 4 was changed to −0.15.

Location (x, y) km	Model 1 (0, 0)	Model 1 (0, 1.5)	Model 2 (0, 0)	Model 2 (0, 1.5)
Before correction (%)	2.3	15	7.3	27
After correction (%)	8.2	8.5	19	20
Actual (%)	7.5	7.5	18	18

Downloaded 22 May 2012 to 138.67.12.93. Redistribution subject to SEG license or copyright; see Terms of Use at http://segdl.org/

Assuming that z'_{TL}/z and z'_{RL}/z are known from vertical traveltimes, the total lens-induced traveltime shift for the reflection from the bottom of the target can be computed as

$$\Delta t_{\rm ta} = \frac{1}{2}\left(\frac{\Delta t_0(\mathbf{x}_{TL})}{\cos\theta_{TL}} + \frac{\Delta t_0(\mathbf{x}_{RL})}{\cos\theta_{TL}}\right), \qquad (27)$$

where $\Delta t_0(\mathbf{x}_{TL})$ and $\Delta t_0(\mathbf{x}_{RL})$ are the zero-offset time distortions below the lens at locations $\mathbf{x}_{TL}$ and $\mathbf{x}_{RL}$, respectively.

After the correction, the reflection traveltimes should be close to those in the background model and, therefore, well-described by equation 20. The interval values of $V_{\rm nmo}^{(1,2)}$ and $\eta^{(1,2,3)}$ can be computed following the algorithm of Wang and Tsvankin (2009) using the layer-stripped data corrected for the lens-induced time shifts. The removal of the LH-related time distortions should also improve stacking of wide-azimuth data.

The horizontal coordinates $\mathbf{x}_{TL}$ and $\mathbf{x}_{RL}$ for the longest-offset raypath for each azimuth delineate the area corresponding to the effective spreadlength $L'(\alpha)$. That area can be used to find the second traveltime derivatives needed in the analytic correction of the NMO ellipse discussed above.

Synthetic tests

The correction algorithm was tested on the layered model from Table 6 that includes a lens embedded in a three-layer orthorhombic medium. The moveout parameters $V_{\rm nmo}^{(1,2)}$, φ, and $\eta^{(1,2,3)}$ were estimated at the center and side of the lens from finite-difference synthetic data. The required input quantities for the lens correction are the vertical-time distortion Δt_0 in the lens area, the horizontal coordinates $\mathbf{x}_{TL}$ and $\mathbf{x}_{RL}$ for each reflected ray, and the angles θ_{TL} and θ_{RL}. The spatially varying values Δt_0 were obtained from the pull-up anomaly measured from near-offset stacked data (Figure 15). The spatial extent of the lens can be also identified by the high-amplitude anomaly of the reflection from its top. The pull-up time anomaly is observed for the bottom of the lens layer as well as for interfaces 3 and 4. The agreement of the spatial extent of the amplitude and zero-offset time anomalies can be used to identify an LH layer on field data (Armstrong et al., 2001; Takanashi et al., 2008, 2009a).

The ratio z'/z for the layer containing the lens is not required for estimating the coordinates $\mathbf{x}_{TL}$ and $\mathbf{x}_{RL}$ because the lens in this model is sufficiently close to the bottom of layer 1 (Figure 8). Thus, $\mathbf{x}_{TL} \approx \mathbf{x}_{T1}$ and $\mathbf{x}_{RL} \approx \mathbf{x}_{R1}$ can be obtained by matching the time slopes of the target reflection and the reflection from the bottom of layer 1 (Figure 8).

The gather uncorrected for LH contains azimuthally varying residual moveout, which could not be removed by the nonhyperbolic moveout equation 20 (Figure 16a). Application of traveltime shifts substantially reduces the residual moveout and makes it possible to produce a high-quality stack.

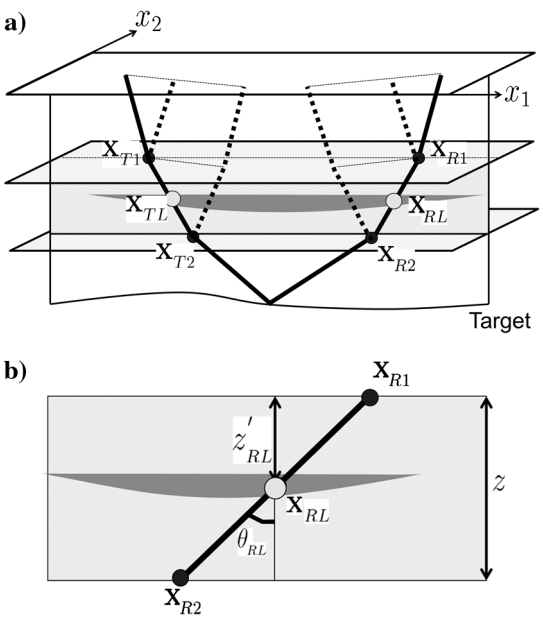

Figure 14. (a) 3D ray diagram of the correction algorithm. The horizontal coordinates of the intersection points (two-component vectors $\mathbf{x}_{T1}$, $\mathbf{x}_{T2}$, $\mathbf{x}_{R1}$, and $\mathbf{x}_{R2}$) are determined from velocity-independent layer stripping. (b) An upgoing ray segment crossing the lens. Using the values of z'_{RL} and z, we can compute the horizontal location of the crossing point ($\mathbf{x}_{RL}$) and the ray angle (θ_{RL}) with the vertical.

Table 6. Anisotropy parameters of a layered orthorhombic model with an isotropic velocity lens in layer 2. The model geometry and the vertical velocity V_0 are the same as in Figure 8 (V_0 in the second layer is shown in Figure 8b). The angle φ is the azimuth of the $[x_1, x_3]$ symmetry plane.

	Layer 1	Layer 2	Layer 3	Layer 4
$V_{\rm nmo}^{(1)}$ (km/s)	2.0	2.5–3.3	3.8	4.72
$V_{\rm nmo}^{(2)}$ (km/s)	1.9	2.5–3.3	4.0	4.85
φ (degrees)	−45	—	−45	−45
$\eta^{(1)}$	0	0	0.05	0
$\eta^{(2)}$	0	0	0	0.07
$\eta^{(3)}$	0	0	0.1	−0.12

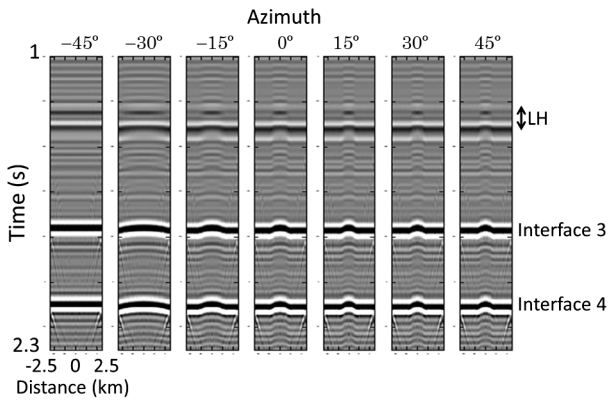

Figure 15. Near-offset stacked sections for several azimuthal directions. The center of each panel corresponds to $x = y = 0$. The azimuth −45° corresponds to the major axis of the lens.

Downloaded 22 May 2012 to 138.67.12.93. Redistribution subject to SEG license or copyright; see Terms of Use at http://segdl.org/

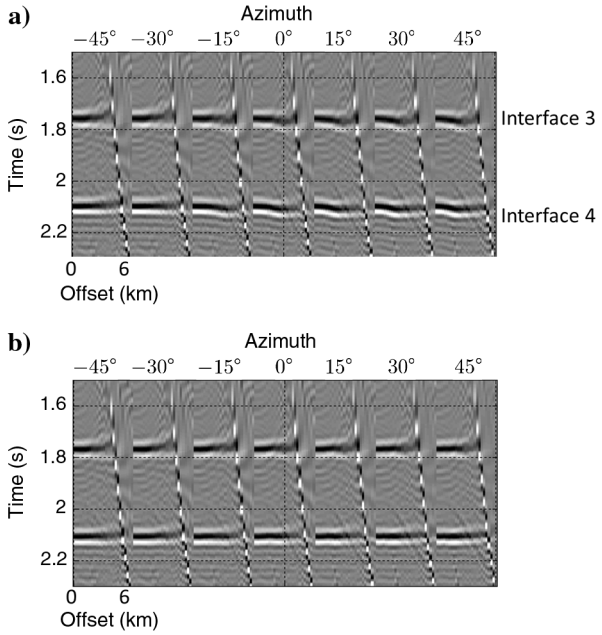

Figure 16. CMP gathers in different azimuthal directions at the center of the lens. The gathers are corrected for nonhyperbolic moveout using equation 20 (a) before and (b) after applying the lens-related traveltime shifts.

Table 7. Estimated interval parameters $V_{nmo}^{(1,2)}$, φ, and $\eta^{(1,2,3)}$ in layer 4 from the model in Table 6 before and after applying the time shifts (equation 27).

Location (x, y) km	Actual	Before correction (0, 0)	After correction (0, 0)	Before correction (0, 1.5)	After correction (0, 1.5)
$V_{nmo}^{(1)}$ (km/s)	4.72	3.58	4.79	5.07	4.70
$V_{nmo}^{(2)}$ (km/s)	4.85	4.59	4.93	5.05	4.87
φ (degrees)	45	45	45	—	45
$\eta^{(1)}$	0	0.49	−0.01	0.04	0.01
$\eta^{(2)}$	0.07	0.22	0.04	0.05	0.05
$\eta^{(3)}$	−0.12	0.13	−0.10	0.46	−0.15

Next, the interval parameters $V_{nmo}^{(1,2)}$ and $\eta^{(1,2,3)}$ for layer 4 are estimated using the layer-stripped prestack data, as suggested by Wang and Tsvankin (2009). The errors in $V_{nmo}^{(1)}$ and $\eta^{(1)}$ before the lens correction reach 25% and 0.49, respectively; after the correction, the distortion is reduced to 1% for $V_{nmo}^{(1,2)}$ and less than 0.03 for $\eta^{(1,2,3)}$ (Table 7). As shown in Takanashi and Tsvankin (2011) for 2D models, errors up to 20% in the input parameters Δt_0 and z do not significantly impair the correction results.

CONCLUSIONS

We presented an analytic expression for the NMO ellipse in a stratified anisotropic medium with an arbitrary number of laterally heterogeneous (LH) layers. Both anisotropy and heterogeneity are assumed to be weak, and the horizontal plane has to be a plane of symmetry. The equation shows that the distortion caused by an LH layer in the overburden is proportional to the quadratic lateral variation of the interval vertical traveltime and also increases with target depth and average effective NMO velocity for the target event.

Because of the strong depth dependence of the influence of lateral heterogeneity, application of the generalized Dix equation may significantly amplify the false elongation or compression of the effective NMO ellipses. To obtain an accurate interval NMO ellipse in the reference homogeneous medium, the influence of LH on the effective NMO ellipses should be removed before applying Dix differentiation. The correction for lateral heterogeneity requires estimating the second horizontal derivatives of the vertical traveltime in the LH interval and the circular (isotropic) approximations for the interval NMO velocity in all layers.

The presented equation can be applied to multiple LH layers by computing the horizontal interval traveltime derivatives for each layer. Since the influence of weak anisotropy on the correction term is negligible, the method is not restricted to HTI and remains valid for lower-symmetry (orthorhombic and monoclinic) media with a horizontal symmetry plane. Synthetic tests confirm the accuracy of our formalism for typical horizontally layered models with moderate anisotropy and lateral velocity variation. Although the correction for LH substantially reduces the distortion in the interval moveout, Dix differentiation is sensitive to even small errors in the effective NMO ellipses, particularly when the target interval is relatively thin.

To describe NMO ellipses for interfaces beneath thin velocity lenses, we compute the second lateral traveltime derivatives by approximating the zero-offset traveltime with a quadratic function over the area corresponding to the effective spreadlength (i.e., to the maximum distance between the incident and reflected rays at lens depth). Application of our technique to isotropic and HTI models showed that it closely approximates the laterally varying lens-induced distortion in the effective NMO ellipses. Consequently, generalized Dix differentiation produces an accurate interval NMO ellipse in the reference homogeneous model. Although this analytic approach cannot be used to correct prestack traveltimes and increase stack power, it helps quickly evaluate the influence of velocity lenses on both effective and interval NMO velocities and reconstruct the background NMO ellipticities.

To correct long-offset, multiazimuth prestack data for lens-induced time shifts, we developed an approach based on 3D velocity-independent layer stripping (VILS). The correction algorithm assumes that the raypath perturbation caused by the lens is negligible and requires estimates of the lens-related zero-offset time distortion Δt_0, the thickness of the layer containing the lens, and the distance between the lens and the nearest layer boundary. The method was successfully tested on synthetic data generated with a finite-difference algorithm for a thin lens embedded in a layered orthorhombic medium. Application of prestack traveltime shifts substantially reduced errors in the effective and interval moveout parameters $V_{nmo}^{(1,2)}$ and $\eta^{(1,2,3)}$ and ensured a high quality of stack for a wide range of offsets and azimuths.

Since some fractured reservoirs are overlaid by a gently dipping overburden containing velocity lenses, the developed methodology

Downloaded 22 May 2012 to 138.67.12.93. Redistribution subject to SEG license or copyright; see Terms of Use at http://segdl.org/

should be highly beneficial in fracture-detection projects. The proposed correction algorithms should also help build more accurate velocity models for imaging of wide-azimuth offshore data.

ACKNOWLEDGMENTS

We are grateful to M. Al-Chalabi (Petrotech Consultancy), T. Alkhalifah (KAUST), E. Blias (VSFusion), T. Davis (CSM), V. Grechka (Marathon), E. Jenner (ION/GXT), W. Lynn (Lynn Inc.), and to members of the A(nisotropy)-Team of the Center for Wave Phenomena (CWP) at Colorado School of Mines (CSM) for helpful discussions. We also thank E. Jenner for providing the synthetic data and Jeff Godwin (CWP) for assistance with the Madagascar software package. This work was supported by Japan Oil, Gas and Metals National Corporation (JOGMEC) and the Consortium Project on Seismic Inverse Methods for Complex Structures at CWP.

APPENDIX A

NMO ELLIPSE IN A HORIZONTALLY LAYERED MODEL WITH WEAK LATERAL VELOCITY VARIATION

The goal of this appendix is to obtain an approximate expression for the NMO ellipse in a stratified model with an arbitrary number of laterally heterogeneous layers. First, we derive the NMO ellipse for an N-layer model with lateral heterogeneity confined to layer m (Figure A-1). The derivation follows the approach of Grechka and Tsvankin (1999, Appendix B), whose model was limited to two LH layers. The magnitude of anisotropy in each layer and of lateral heterogeneity in layer m is assumed to be weak, and the horizontal plane is taken to be a plane of symmetry. In the linear approximation, the raypath perturbation caused by lateral heterogeneity can be neglected, so the ray does not deviate from the vertical incidence plane (Figure A-1).

Then the one-way traveltime $\tau^{\text{het}}(x_1, x_2)$ for the stratified model from Figure A-1 can be obtained in the same way as in Grechka and Tsvankin (1999, equation B-3):

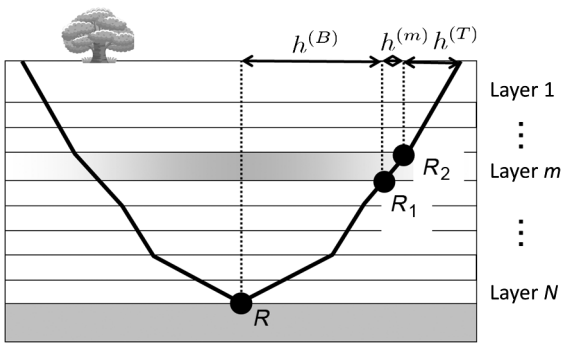

Figure A-1 Reflection raypath through an anisotropic, horizontally layered model. The half-offset $h = h^{(B)} + h^{(m)} + h^{(T)}$; R is the reflection point for the unperturbed ray, and R_1 and R_2 are the intersection points with layer boundaries. The raypath perturbation caused by weak lateral heterogeneity is assumed to be negligible, and the ray is confined to the vertical plane. Only layer m is laterally heterogeneous.

$$\tau^{\text{het}}(x_1, x_2) = \tau_T + \tau_B + \frac{\sqrt{(h^{(m)})^2 + (z^{(m)})^2}}{h^{(m)}} \times \int_{h^{(B)}}^{h^{(m)}+h^{(B)}} \frac{1}{g^{(m)}(\xi)}\, d\xi, \tag{A-1}$$

where

$$h^{(B)} = h^{(m+1)} + \cdots + h^{(N)}, \tag{A-2}$$

$$\tau_T = \tau_1 + \cdots + \tau_{m-1}, \tag{A-3}$$

and

$$\tau_B = \tau_{m+1} + \cdots + \tau_N. \tag{A-4}$$

Here ξ is the horizontal displacement along the ray, $\tau_{1\ldots N}$ is the one-way interval traveltime, and $z^{(m)}$ is the thickness of layer m.

The interval group velocity along the ray is denoted by $g^{(m)} = g^{(m)}(\alpha, \theta, \xi) = g^{(m)}(\alpha, \theta, y_1, y_2)$ (α is the azimuth of the CMP line, and θ is the polar angle). As mentioned above, the traveltime perturbation due to the velocity variation is computed along the unperturbed ray in the laterally homogeneous layered model. Expanding the lateral variation of $g^{(m)}$ in a double Taylor series in the horizontal coordinates y_1 and y_2 and evaluating the integral in equation A-1, τ^{het} can be expressed as (Grechka and Tsvankin, 1999, Appendix B):

$$\tau^{\text{het}} = \tau_T + \tau_B + \tau_m^{\text{hom}} \left[1 - \frac{\frac{h^{(m)}}{h} + 2\frac{h^{(B)}}{h}}{2g_0^{(m)}} (g_{,1}^{(m)} x_1 + g_{,2}^{(m)} x_2) - \frac{(\frac{h^{(m)}}{h}) + 3\frac{h^{(m)}h^{(B)}}{h^2} + 3(\frac{h^{(B)}}{h})^2}{6g_0^{(m)}} \times (g_{,11}^{(m)} x_1^2 + 2g_{,12}^{(m)} x_1 x_2 + g_{,22}^{(m)} x_2^2) \right], \tag{A-5}$$

where τ_m^{hom} is the one-way interval traveltime for the reference homogeneous model, $x_1 = h\cos\alpha$, $x_2 = h\sin\alpha$, and $g_0^{(m)}$, $g_{,i}^{(m)}$, and $g_{,ij}^{(m)}$ are the zero-, first-, and second-order terms of the Taylor series:

$$g_0^{(m)} \equiv g^{(m)}(\alpha, \theta, 0, 0), \tag{A-6}$$

$$g_{,i}^{(m)} \equiv \left. \frac{\partial g^{(m)}(\alpha, \theta, y_1, y_2)}{\partial y_i} \right|_{y_1 = y_2 = 0}, \tag{A-7}$$

$$g_{,ij}^{(m)} \equiv \left. \frac{\partial^2 g^{(m)}(\alpha, \theta, y_1, y_2)}{\partial y_i\, \partial y_j} \right|_{y_1 = y_2 = 0}. \tag{A-8}$$

The third- and higher-order terms are assumed to be negligible.

If anisotropy and lateral heterogeneity are weak, Snell's law at the transmission points can be applied to the background

Downloaded 22 May 2012 to 138.67.12.93. Redistribution subject to SEG license or copyright; see Terms of Use at http://segdl.org/

group velocities $g^{(m)}|_{y_1=y_2=0}$ (for layer $m = 1, 2, ..., N$) and the corresponding ray angles (Figure A-1):

$$\frac{\sin\theta_1}{g^{(1)}} = \frac{\sin\theta_2}{g^{(2)}} = \cdots = \frac{\sin\theta_m}{g^{(m)}} = \cdots = \frac{\sin\theta_N}{g^{(N)}}. \quad \text{(A-9)}$$

Since the LH-induced raypath perturbation is neglected, equation A-9 can be rewritten as

$$\frac{h^{(1)}}{\tau_1^{\text{hom}}(g^{(1)})^2} = \frac{h^{(2)}}{\tau_2^{\text{hom}}(g^{(2)})^2} = \cdots = \frac{h^{(m)}}{\tau_m^{\text{hom}}(g^{(m)})^2} = \cdots = \frac{h^{(N)}}{\tau_N^{\text{hom}}(g^{(N)})^2}, \quad \text{(A-10)}$$

which leads to the following relationships:

$$\frac{h^{(m)}}{h} = \frac{\tau_m(g^{(m)})^2}{\sum_{r=1}^{N}\tau_r(g^{(r)})^2} \quad \text{(A-11)}$$

and

$$\frac{h^{(B)}}{h} = \frac{\sum_{r=m+1}^{N}\tau_r(g^{(r)})^2}{\sum_{r=1}^{N}\tau_r(g^{(r)})^2}. \quad \text{(A-12)}$$

In the weak-anisotropy approximation, the vertical velocities $g_0^{(m)}$ can be replaced with the interval NMO velocities averaged over azimuth (Grechka and Tsvankin, 1999):

$$V_{\text{cir}}^{-2} = \frac{1}{2\pi}\int_0^{2\pi} V_{\text{nmo}}^{-2}(\alpha)d\alpha = \frac{W_{11}^{\text{hom}} + W_{22}^{\text{hom}}}{2} \approx \frac{W_{11}^{\text{het}} + W_{22}^{\text{het}}}{2}. \quad \text{(A-13)}$$

Therefore, the ratios $k_m = \frac{h^{(m)}}{h}\Big|_{h=0}$ and $l_m = \frac{h^{(B)}}{h}\Big|_{h=0}$ are determined by $V_{\text{cir}}^{(m)}$ and the vertical traveltimes τ_{0m}:

$$k_m = \frac{\tau_{0m}(V_{\text{cir}}^{(m)})^2}{\sum_{r=1}^{N}\tau_{0r}(V_{\text{cir}}^{(r)})^2} = \frac{\tau_{0m}(V_{\text{cir}}^{(m)})^2}{\tau_{0T}(V_{\text{cir}}^{(T)})^2 + \tau_{0m}(V_{\text{cir}}^{(m)})^2 + \tau_{0B}(V_{\text{cir}}^{(B)})^2}, \quad \text{(A-14)}$$

and

$$l_m = \frac{\sum_{r=m+1}^{N}\tau_{0r}(V_{\text{cir}}^{(r)})^2}{\sum_{r=1}^{N}\tau_{0r}(V_{\text{cir}}^{(r)})^2} = \frac{\tau_{0B}(V_{\text{cir}}^{(B)})^2}{\tau_{0T}(V_{\text{cir}}^{(T)})^2 + \tau_{0m}(V_{\text{cir}}^{(m)})^2 + \tau_{0B}(V_{\text{cir}}^{(B)})^2}, \quad \text{(A-15)}$$

where $V_{\text{cir}}^{(T)}$ and $V_{\text{cir}}^{(B)}$ are the circular approximations of the interval NMO velocities in the layers above (from 1 to $m-1$) and below (from $m+1$ to N) the LH layer, respectively, and τ_{0T} and τ_{0B} are corresponding zero-offset traveltimes. Evaluating the second-order derivatives of equation A-5 with respect to x_1 and x_2 at the CMP location yields:

$$\begin{aligned}\frac{\partial^2\tau^{\text{het}}}{\partial x_i\partial x_j}\Big|_{\mathbf{x}=0} &= \frac{\partial^2\tau^{\text{hom}}}{\partial x_i\partial x_j}\Big|_{\mathbf{x}=0} \\ &- (k_m + 2l_m)\left[\frac{\partial\tau_m^{\text{hom}}}{\partial x_i}\Big|_{\mathbf{x}=0}\frac{g_{,j}^{(m)}}{g_0^{(m)}} + \frac{\partial\tau_m^{\text{hom}}}{\partial x_j}\Big|_{\mathbf{x}=0}\frac{g_{,i}^{(m)}}{g_0^{(m)}}\right] \\ &- \tau_m^{\text{hom}}(k_m + 2l_m)\left[\frac{\partial}{\partial x_i}\left(\frac{g_{,j}^{(m)}}{g_0^{(m)}}\right) + \frac{\partial}{\partial x_j}\left(\frac{g_{,i}^{(m)}}{g_0^{(m)}}\right)\right]\Big|_{\mathbf{x}=0} \\ &- \tau_{0m}^{\text{hom}}\frac{(k_m^2 + 3k_m l_m + 3l_m^2)\,g_{,ij}^{(m)}}{3g_0^{(m)}}\Big|_{\mathbf{x}=0}. \end{aligned} \quad \text{(A-16)}$$

Following Grechka and Tsvankin (1999, Appendices A and B), we eliminate the terms containing $\partial\tau_m^{\text{hom}}/\partial x_{(i,j)}$ (since the zero-offset ray is assumed to be vertical, and the interval traveltime is symmetric with respect to the vertical axis) and $g_{,(i,j)}^{(m)}$ (because of the symmetry with respect to the vertical axis). Then equation A-16 yields

$$\frac{\partial^2\tau^{\text{het}}}{\partial x_i\partial x_j}\Big|_{\mathbf{x}=0} = \frac{\partial^2\tau^{\text{hom}}}{\partial x_i\partial x_j}\Big|_{\mathbf{x}=0} - \left[\frac{k_m^2 + 3k_m l_m + 3l_m^2}{3g_0^{(m)}}\tau_{0m}^{\text{hom}}\,g_{,ij}^{(m)}\right]. \quad \text{(A-17)}$$

Using the definition of the NMO ellipse (Grechka and Tsvankin, 1998) and setting $\tau_{0m} = \tau_{0m}^{\text{het}} = \tau_{0m}^{\text{hom}}$ (because lateral heterogeneity is weak), equation A-17 can be rewritten as

$$W_{ij}^{\text{het}} = W_{ij}^{\text{hom}} - \frac{\tau_0}{3g_0^{(m)}}\left[(k_m^2 + 3k_m l_m + 3l_m^2)\tau_{0m}g_{,ij}^{(m)}\right]\Big|_{\mathbf{x}=0}, \quad (i, j = 1, 2), \quad \text{(A-18)}$$

where W_{ij}^{het} is the NMO ellipse for the actual model, and W_{ij}^{hom} is the NMO ellipse for the reference anisotropic homogeneous medium. Since all reflectors in the model are horizontal, the second spatial derivatives of the vertical velocity $g_0^{(m)}$ can be approximately expressed through those of the vertical traveltime τ_{0m} (Grechka and Tsvankin, 1999)

$$W_{ij}^{\text{hom}} = W_{ij}^{\text{het}} - \frac{\tau_0}{3}\left[(k_m^2 + 3k_m l_m + 3l_m^2)\tau_{0m,ij}\right]\Big|_{\mathbf{x}=0}, \quad (i, j = 1, 2). \quad \text{(A-19)}$$

Note that the Taylor-series expansion of the group velocity $g_0^{(m)}$ used in the derivation can be replaced with that of the "group slowness" (the inverse of $g_0^{(m)}$). Then equation A-19 can be derived without applying the linear approximation to equation A-18 required to obtain $1/(g^{(m)}(\alpha, \theta, y_1, y_2))$ from $g^{(m)}(\alpha, \theta, y_1, y_2)$ (Grechka and Tsvankin, 1999, their equation A-11). Numerical testing shows that the expression for the heterogeneity-related term in equation A-19 (with the second derivatives of the interval vertical traveltime) is more accurate than that in equation A-18 (with the second derivatives of the interval vertical velocity).

Downloaded 22 May 2012 to 138.67.12.93. Redistribution subject to SEG license or copyright; see Terms of Use at http://segdl.org/

As mentioned above, in the linear approximation the raypath perturbation caused by weak lateral heterogeneity can be ignored. Therefore, equation A-19 can be generalized for a model with an arbitrary number of LH layers (i.e., every layer can be LH) as follows:

$$W_{ij}^{\mathrm{hom}} = W_{ij}^{\mathrm{het}} - \sum_{m=1}^{N} \frac{\tau_0 D_m}{3} \frac{\partial^2 \tau_{0m}}{\partial y_i \partial y_j}\bigg|_{\mathbf{y}=\mathbf{y}_{\mathrm{CMP}}}, \quad (i,j=1,2), \tag{A-20}$$

where

$$D_m = k_m^2 + 3k_m l_m + 3l_m^2. \tag{A-21}$$

REFERENCES

Alkhalifah, T., and I. Tsvankin, 1995, Velocity analysis for transversely isotropic media: Geophysics, **60**, 1550–1566, doi: 10.1190/1.1443888.

Armstrong, T., J. McAteer, and P. Connolly, 2001, Removal of overburden velocity anomaly effects for depth conversion: Geophysical Prospecting, **49**, 79–99, doi: 10.1046/j.1365-2478.2001.00238.x.

Bakulin, A., V. Grechka, and I. Tsvankin, 2000a, Estimation of fracture parameters from reflection seismic data — Part I: HTI model due to a single fracture set: Geophysics, **65**, 1788–1802, doi: 10.1190/1.1444863.

Bakulin, A., V. Grechka, and I. Tsvankin 2000b, Estimation of fracture parameters from reflection seismic data — Part II: Fractured models with orthorhombic symmetry: Geophysics, **65**, 1803–1817, doi: 10.1190/1.1444864.

Biondi, B., 2006, 3D seismic imaging: SEG.

Blias, E., 2009, Stacking velocities in the presence of overburden velocity anomalies: Geophysical Prospecting, **57**, 323–341, doi: 10.1111/gpr.2009.57.issue-3.

Calvert, A., E. Jenner, R. Jefferson, R. Bloor, N. Adams, R. Ramkhelawan, and C. S. Clair, 2008, Preserving azimuthal velocity information: Experiences with cross-spread noise attenuation and offset vector tile PreSTM: 78th Annual International Meeting, SEG, Expanded Abstracts, 207–211.

Cary, P. W., 1999, Common-offset-vector gathers: An alternative to cross-spreads for wide-azimuth 3D surveys: 69th Annual International Meeting, SEG, Expanded Abstracts, 1496–1499.

Dewangan, P., and I. Tsvankin, 2006, Velocity-independent layer stripping of PP and PS reflection traveltimes: Geophysics, **71**, no. 4, U59–U65.

Grechka, V., and I. Tsvankin, 1998, 3D description of normal moveout in anisotropic inhomogeneous media: Geophysics, **63**, 1079–1092, doi: 10.1190/1.1444386.

Grechka, V., and I. Tsvankin, 1999, 3D moveout inversion in azimuthally anisotropic media with lateral velocity variation: Theory and a case study: Geophysics, **64**, 1202–1218, doi: 10.1190/1.1444627.

Grechka, V., I. Tsvankin, and J. K. Cohen, 1999, Generalized Dix equation and analytic treatment of normal-moveout velocity for anisotropic media: Geophysical Prospecting, **47**, 117–148, doi: 10.1046/j.1365-2478.1999.00120.x.

Jenner, E., 2009, Data example and modelling study of P-wave azimuthal anisotropy potentially caused by isotropic velocity heterogeneity: First Break, **27**, 45–50.

Jenner, E., 2010, Modelling azimuthal NMO in laterally heterogeneous HTI media: First Break, **28**, 89–94.

Jenner, E., M. Williams, and T. Davis, 2001, A new method for azimuthal velocity analysis and application to a 3D survey, Weyburn field, Saskatchewan, Canada: 71st Annual International Meeting, SEG, Expanded Abstracts, 102–105.

Koren, Z., and I. Ravve, 2011, Full-azimuth subsurface angle domain wavefield decomposition and imaging Part I: Directional and reflection image gathers: Geophysics, **76**, no. 1, S1–S13, doi: 10.1190/1.3511352.

Luo, M., M. Takanashi, K. Nakayama, and T. Ezaka, 2007, Physical modeling of overburden effects: Geophysics, **72**, no. 4, T37–T45, doi: 10.1190/1.2735925.

Lynn, H. B., 2004a, The winds of change: The Leading Edge, **23**, 1156–1162, doi: 10.1190/1.1825938.

Lynn, H. B., 2004b, The winds of change: Anisotropic rocks, their preferred direction of fluid flow and their associated seismic signatures — Part 2: The Leading Edge, **23**, 1258–1268, doi: 10.1190/1.1843372.

Melo, G., and P. Sava, 2009, Resolution analysis of wide-azimuth angle decomposition for wave-equation migration: 79th Annual International Meeting, SEG, Expanded Abstracts, 2904–2908.

Pech, A., and I. Tsvankin, 2004, Quartic moveout coeffecient for a dipping azimuthally anisotropic layer: Geophysics, **69**, 699–707, doi: 10.1190/1.1759456.

Sava, P., and I. Vlad, 2011, Wide-azimuth angle gathers for wave-equation migration: Geophysics, **76**, no. 3, S131–S141, doi: 10.1190/1.3560519.

Takanashi, M., M. Fujimoto, and D. Chagalov, 2009a, Overburden heterogeneity effects in migration velocity analysis: A case study in an offshore Australian field: 71st Annual Conference and Exhibition, EAGE, Extended Abstracts.

Takanashi, M., M. Kaneko, N. Monzawa, S. Imahori, T. Ishibashi, and A. Sakai, 2008, Removal of overburden channel effects through channel velocity modeling and prestack depth migration for an oil field offshore Abu-Dhabi: Abu Dhabi International Petroleum Exhibition and Conference, SPE 117982.

Takanashi, M., I. Takahashi, and K. Akama, 2009b, An application of seismic azimuthal anisotropy using land 3D seismic data: Journal of the Japanese Association for Petroleum Technology, **74**, 23–28 (in Japanese).

Takanashi, M., and I. Tsvankin, 2011, Correction for the influence of velocity lenses on nonhyperbolic moveout inversion for VTI media: Geophysics, **76**, no. 3, WA13–WA21, doi: 10.1190/1.3569799.

Tod, S., B. Taylor, R. Johnston, and T. Allen, 2007, Fracture prediction from wide-azimuth land seismic data in SE Algeria: The Leading Edge, **26**, 1154–1160, doi: 10.1190/1.2780786.

Tsvankin, I., 1997, Anisotropic parameters and P-wave velocity for orthorhombic media: Geophysics, **62**, 1292–1309, doi: 10.1190/1.1444231.

Tsvankin, I., 2005, Seismic signatures and analysis of reflection data in anisotropic media, 2nd edition: Elsevier Science Publishing Company, Inc.

Tsvankin, I., J. Gaiser, V. Grechka, M. van der Baan, and L. Thomsen, 2010, Seismic anisotropy in exploration and reservoir characterization: An overview: Geophysics, **75**, no. 5, 75A15–75A29, doi: 10.1190/1.3481775.

Tsvankin, I., and V. Grechka, 2011, Seismology of azimuthally anisotropic media and seismic fracture characterization: SEG.

Vasconcelos, I., and I. Tsvankin, 2006, Non-hyperbolic moveout inversion of wide-azimuth P-wave data for orthorhombic media: Geophysical Prospecting, **54**, 535–552, doi: 10.1111/j.1365-2478.2006.00559.x.

Vermeer, G. J. O., 2002, 3D seismic survey design: SEG.

Wang, X., and I. Tsvankin, 2009, Estimation of interval anisotropy parameters using velocity-independent layer stripping: Geophysics, **74**, no. 5, WB117–WB127, doi: 10.1190/1.3157462.

Xu, X., and I. Tsvankin, 2006, Anisotropic geometrical-spreading correction for wide-azimuth P-wave reflections: Geophysics, **71**, no. 5, D161–D170, doi: 10.1190/1.2335615.

Downloaded 22 May 2012 to 138.67.12.93. Redistribution subject to SEG license or copyright; see Terms of Use at http://segdl.org/